ACS MATERIALS Au
AN OPEN ACCESS JOURNAL OF THE AMERICAN CHEMICAL SOCIETY

pubs.acs.org/materialsau Article

Path Less Traveled: A Contemporary Twist on Synthesis and Traditional Structure Solution of Metastable $LiNi_{12}B_8$

Gourab Bhaskar, Volodymyr Gvozdetskyi, Scott L. Carnahan, Renhai Wang, Aishwarya Mantravadi, Xun Wu, Raquel A. Ribeiro, Wenyu Huang, Aaron J. Rossini, Kai-Ming Ho, Paul C. Canfield, Oleg I. Lebedev, and Julia V. Zaikina*

Cite This: *ACS Mater. Au* 2022, 2, 614–625

Read Online

ACCESS | Metrics & More | Article Recommendations | Supporting Information

ABSTRACT: Achieving kinetic control to synthesize metastable compounds is a challenging task, especially in solid-state reactions where the diffusion is slow. Another challenge is the unambiguous crystal structure determination for metastable compounds when high-quality single crystals suitable for single-crystal X-ray diffraction are inaccessible. In this work, we report an unconventional means of synthesis and an effective strategy to solve the crystal structure of an unprecedented metastable compound $LiNi_{12}B_8$. This compound can only be produced upon heating a metastable layered boride, *HT*-$Li_{0.4}NiB$ (*HT*: high temperature), in a sealed niobium container. A conventional heating and annealing of elements do not yield the title compound, which is consistent with the metastable nature of $LiNi_{12}B_8$. The process to crystallize this compound is sensitive to the annealing temperature and dwelling time, a testament to the complex kinetics involved in the formation of the product. The unavailability of crystals suitable for single-crystal X-ray diffraction experiments prompted solving the crystal structure from high-resolution synchrotron powder X-ray diffraction data. This compound crystallizes in a new structure type with space group *I*4/*mmm* (a = 10.55673(9) Å, c = 10.00982(8) Å, V = 1115.54(3) Å^3, Z = 6). The resulting complex crystal structure of $LiNi_{12}B_8$ is confirmed by scanning transmission electron microscopy and solid-state ^{11}B and ^{7}Li NMR spectroscopy analyses. The extended Ni framework with Li/Ni disorder in its crystal structure resulted in the spin-glass or cluster glass type magnetic ordering below 24 K. This report illustrates a "contemporary twist" to traditional methodologies toward synthesizing a metastable compound and provides a recipe for solving structures by combining the complementary characterization techniques in the cases where the traditionally used single-crystal X-ray diffraction method is nonapplicable.

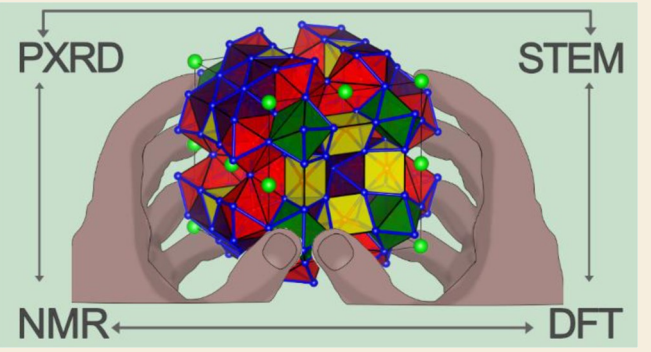

KEYWORDS: *lithium, transition metal, boron, kinetically stabilized phase, metastable compound, in situ XRD, STEM, solid-state NMR, DFT, MBene*

1. INTRODUCTION

The outcome of a chemical reaction depends on whether the reaction pathway is thermodynamically or kinetically controlled. Thermodynamically controlled pathways often have higher activation energies and yield products with the lowest free energies. On the contrary, the activation energy for a kinetically controlled pathway is typically lower, thus leading to products that rapidly form but do not have the lowest energies. A traditional solid-state synthesis that involves the direct combination of solid elemental precursors has to be performed at elevated temperatures for an extended time to overcome the high diffusion barriers between inorganic solids. Such prolonged heat treatment often directs the reactions along a thermodynamically controlled pathway hindering access to metastable (kinetically stabilized) compounds. Therefore, for the synthesis of metastable compounds, "turning down the heat" and employing unconventional synthetic routes are shown to be successful strategies to access metastable compounds with potentially unprecedented topology and properties.[1−12]

Recent advancements toward gaining kinetic control through metathesis,[12−20] low-temperature solution synthesis,[21−28] and chimie douce (soft chemistry)[29−35] have allowed metastable compounds to become readily accessible. When it comes to borides, the challenge of synthesizing metastable borides is even greater due to the high melting point of

Received: April 5, 2022
Revised: May 19, 2022
Accepted: May 27, 2022
Published: June 10, 2022

https://doi.org/10.1021/acsmaterialsau.2c00033
ACS Mater. Au 2022, 2, 614–625

elemental boron (~2350 K), thus requiring unconventional synthetic methods. Rare examples of metastable borides include Na_2BP_2 obtained via an oxidative elimination pathway,[36] β-$NdCo_2B_2$ synthesized via rapid cooling of an arc-melted ingot,[37] and Ni_7B_3 from low-temperature solution synthesis,[22] making metastable borides an underexplored class of materials. Motivated by these studies, we pursued the preparation of metastable borides in the Li−Ni−B system through soft topochemical deintercalation route.

Our recent report on two metastable borides, *RT*-$Li_{0.6}$NiB and *HT*-$Li_{0.4}$NiB (*RT*: room temperature; *HT*: high temperature), synthesized upon partial topochemical deintercalation of Li from the layered *RT*-LiNiB and *HT*-LiNiB polymorphs[38] laid a foundation for this study. Crystal structures of both *RT*- and *HT*-LiNiB feature alternating, one-atom-thick [NiB] and Li layers with different topologies.[39] Given their layered structure and labile Li cations, LiNiB polymorphs are suitable precursors for preparing two-dimensional (2D) single-layer borides, *M*Benes (*M* = early transition metals) via Li deintercalation. *M*Benes are boron analogues of 2D carbides/nitrides, *MX*enes. *MX*enes are obtained by topochemical deintercalation of loosely bonded "*A*" atoms from the parent $M_{n+1}AX_n$ (*MAX*) phases (*M* = early transition metals, *A* = elements of groups 13−14 (mainly Al or Si), and *X* = C or N).[40−43] Unlike graphene and *MX*enes, bulk preparation of individual *M*Benes remains in its infancy, although there are a few appropriate deintercalable precursors. Nevertheless, *M*Benes have been theoretically predicted to have outstanding properties as battery materials, catalysts, and magnetic materials,[44−47] and several attempts have been made to synthesize them.[48−52]

Motivated by the intriguing properties of *M*Benes and the successful partial Li-deintercalation from LiNiB, we attempted the complete Li deintercalation at elevated temperatures to obtain individual *M*Bene (NiBene) layers. Unexpectedly, heating *HT*-$Li_{0.4}$NiB leads to a novel metastable boride $LiNi_{12}B_8$ with a new structure type. A thorough analysis of in situ high-temperature synchrotron and ex situ laboratory powder X-ray diffraction (PXRD) data reveals $LiNi_{12}B_8$ to be metastable. Solving the crystal structure of this new compound via the commonly used single-crystal X-ray diffraction method presented a challenge due to the unavailability of large enough and good quality single crystals and the presence of light elements (Li and B) that are weak X-ray scatterers. Therefore, to elucidate the structure of this compound, we used complementary characterization techniques—high-resolution synchrotron PXRD, ^{7}Li and ^{11}B solid-state NMR spectroscopy, scanning transmission electron microscopy (STEM), and density functional theory (DFT). The approach presented here that includes solving structure from PXRD and backing it up by an array of other characterization methods illustrates a "contemporary twist" to traditionally used single-crystal XRD as the only way to determine the structure of a new compound. Finally, magnetic property studies of $LiNi_{12}B_8$ reveal spin glass or cluster glass type magnetic ordering at low temperatures. Overall, this report provides a successful example of a synergistic approach used for the discovery and characterization of a metastable compound and signals about the ample phase space of the metastable compounds that are inaccessible via traditional synthetic routes.

2. EXPERIMENTAL SECTION

2.1. Synthesis

Details about the synthesis of *RT*-LiNiB, *HT*-LiNiB,[39] and their partially Li-deintercalated counterparts *RT*-$Li_{0.6}$NiB and *HT*-$Li_{0.4}$NiB[38] can be found in our recent work. To synthesize nearly phase-pure $LiNi_{12}B_8$, *HT*-LiNiB was first exposed to air for 24 h, washed with deionized (DI) water to remove residual $LiOH{\cdot}H_2O$, and dried under vacuum, followed by repeating this treatment but after 48 h air exposure. Then, 30−60 mg of the dried sample was sealed in an Nb tube, heated to 973 K at a heating rate of 1.4 K/min, dwelled for 12 h, and quenched into cold water.

2.2. Characterization

All polycrystalline samples were characterized by PXRD using a Rigaku MiniFlex600 powder diffractometer with Cu K_α radiation (λ = 1.540593 Å). The thermal stability of *RT*-$Li_{0.6}$NiB, *HT*-$Li_{0.4}$NiB, and $LiNi_{12}B_8$ was investigated by in situ high-temperature synchrotron PXRD collected at the 17-BM beamline at the Advanced Photon Source Argonne National Laboratory (APS ANL) with an average wavelength λ = 0.24141 Å. High-resolution synchrotron PXRD data collected at 11-BM APS ANL at 298 K (λ = 0.45784 Å) were utilized to solve the crystal structure of $LiNi_{12}B_8$. Solid-state ^{7}Li and ^{11}B NMR spectra were acquired using a Bruker Avance III HD spectrometer with a widebore 9.4 T (ν_{1H} = 400 MHz) NMR magnet. Quantitative elemental analysis was carried out via inductively coupled plasma mass spectrometry (ICP-MS) using a Thermo Fisher Scientific X Series 2 ICP-MS. An FEI Quanta-250 field emission scanning electron microscope (SEM) equipped with an Oxford X-Max 80 detector and an Oxford Aztec energy-dispersive X-ray spectroscopy analysis system was utilized for the elemental analysis of the samples. High-angle annular dark field and bright field scanning transmission electron microscopy (HAADF & ABF-STEM) images and electron diffraction (ED) data were acquired using a JEM ARM200F cold FEG double aberration-corrected microscope operated at 200 kV. Magnetic property measurements were performed on the polycrystalline samples using Quantum Design MPMS XL and MPMS3 SQUID magnetometers. First-principles calculations were carried out using DFT within the spin-polarized generalized gradient approximation by the VASP code. Detailed information about the synthesis and characterization methods utilized in this work can be found in the Supporting Information.

3. RESULTS AND DISCUSSION

3.1. NiBene Layers in the Structures of Lithium Nickel Borides

The layered lithium nickel borides *RT*-LiNiB, *HT*-LiNiB, *RT*-Li_{1+x}NiB, and *HT*-Li_{1+y}NiB[39,53] represent a family of layered compounds whose crystal structures are built up of alternating [NiB] and Li layers (Figure 1). These compounds feature different topologies of individual *M*Bene (NiB) and Li layers depending on the temperature and Li "chemical" pressure. We have recently reported[38] on the topochemical deintercalation of Li from both *RT*- and *HT*-LiNiB polymorphs. Images obtained by HAADF-STEM and SEM revealed that deintercalation progresses layer by layer following a "ziplock" mechanism: upon deintercalation of a single Li layer, the "ziplock" is closed, and the adjacent [NiB] layers are forced to condense. However, complete deintercalation of Li could not be achieved by exposure to air, water, ethanol, and dilute HCl at room temperature. Instead, novel metastable borides *RT*-$Li_{0.6}$NiB and *HT*-$Li_{0.4}$NiB form, with complex crystal structures best described as a random intergrowth of ordered $Li[NiB]_n$ (n = 1, 2, 3) substructures with the substructure $Li[NiB]_2$ being the most abundant, accounting for up to 90 mol % in the case of *HT*-$Li_{0.4}$NiB. Considering the metastable nature of the Li-deintercalated products, we hypothesized[54,55] that additional

https://doi.org/10.1021/acsmaterialsau.2c00033
ACS Mater. Au 2022, 2, 614−625

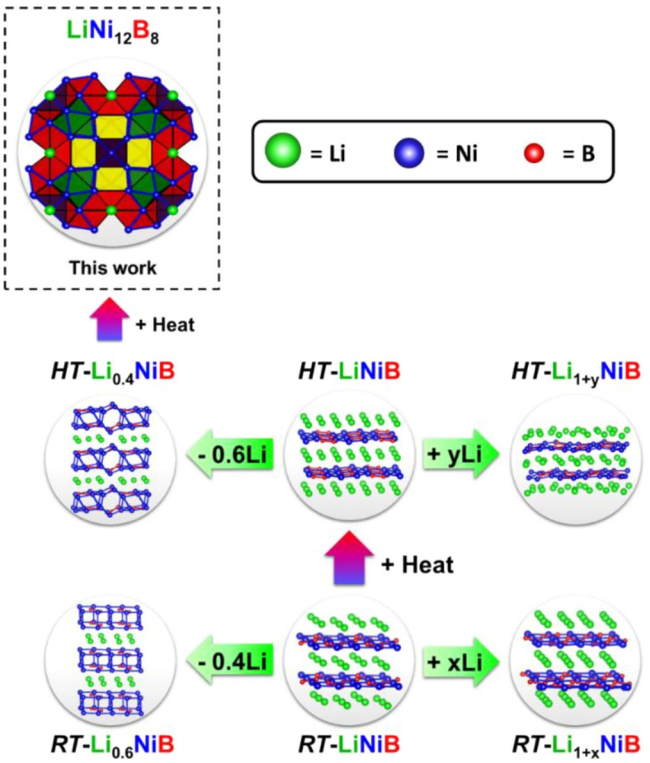

Figure 1. LiNiB phases as flexible platforms to access a plethora of unique layered and nonlayered materials.

thermal energy might lead to further Li deintercalation, accompanied by a possible restructuring or transformation of NiBene layers.

3.2. In Situ and Ex Situ Heating of *RT*-$Li_{0.6}$NiB and *HT*-$Li_{0.4}$NiB

In order to study thermal effects and possible complete deintercalation of Li atoms from *RT*-$Li_{0.6}$NiB and *HT*-$Li_{0.4}$NiB, we acquired in situ and ex situ PXRD data. Both compounds undergo similar transformations under in situ heating (Figures 2, S1, and S2). Upon initial heating, *RT*-$Li_{0.6}$NiB and *HT*-$Li_{0.4}$NiB disproportionate into a Li-rich, *RT*-LiNiB, or *HT*-LiNiB and the Li-depleted compound $LiNi_3B_{1.8}$. Further heating increases the relative peak intensities for $LiNi_3B_{1.8}$ and eventually produces the stable binary borides of nickel (Ni_3B and Ni_4B_3). Interestingly, a few unknown peaks are detected upon heating *RT*-$Li_{0.6}$NiB above 649 K and below 715 K. Rietveld refinement of the PXRD pattern using the *RT*-LiNiB structure as the initial model leads to a new layered *RT**-LiNiB structure (a = 4.552(19) Å, b = 4.844(8) Å, c = 6.38(3) Å, β = 105.80(7)°, and $P2_1/c$), which differs from *RT*-LiNiB (a = 4.61170 Å, b = 4.83330 Å, c = 6.15700 Å, β = 109.61200°, and $P2_1/c$) by the way [NiB] layers are stacked (Figure S3). However, this structure neither could be observed in the ex situ heating of *RT*-$Li_{0.6}$NiB nor quenched to room temperature by rapid cooling. We presume that a side reaction with the silica capillary drives the gradual "leaching" of Li from *RT*-$Li_{0.6}$NiB and *HT*-$Li_{0.4}$NiB phases, leading to the reorganization of the [NiB] layers (Figures 2, S1, and S2):

$$RT\text{-}Li_{0.6}NiB \rightarrow RT\text{-}LiNiB \rightarrow RT^{*}\text{-}LiNiB \rightarrow LiNi_3B_{1.8} \rightarrow Ni_3B,\ Ni_4B_3$$

$$HT\text{-}Li_{0.4}NiB \rightarrow HT\text{-}LiNiB \rightarrow LiNi_3B_{1.8} \rightarrow Ni_4B_3$$

To study only the effect of temperature without a change in composition due to the side reaction, we performed ex situ heating of *RT*-$Li_{0.6}$NiB and *HT*-$Li_{0.4}$NiB in sealed Nb tubes at various temperatures and collected PXRD data after cooling to room temperature. Similar to the in situ heat treatment, both compounds undergo alike transformation upon ex situ heating except for a major difference for *HT*-$Li_{0.4}$NiB between 673 and 1073 K. When the *HT*-$Li_{0.4}$NiB phase is heated at 673 K for 12 h, peaks corresponding to the known ternary compound $LiNi_3B_{1.8}$ along with a few unknown peaks appear in the PXRD pattern (Figure 3). However, when it is heated to 773 K for 12 h, a plethora of unknown peaks are detected, implying a significant transformation of the [NiB] layers within the narrow temperature range of 673−773 K. Because these are broad peaks, indexing of the PXRD pattern is challenging and will be the subject of a future study. Upon heating *HT*-$Li_{0.4}$NiB

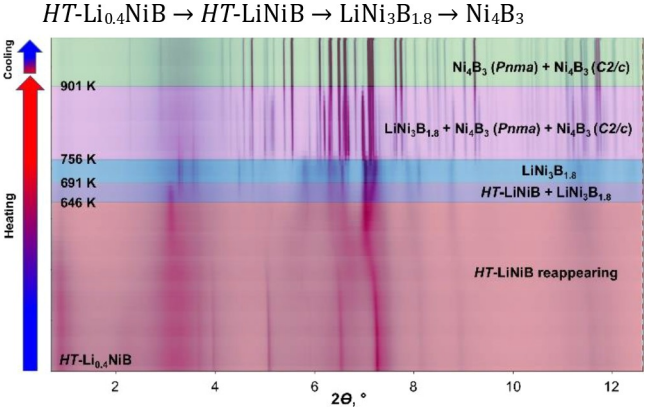

Figure 2. In situ high-temperature synchrotron powder X-ray diffraction data (λ = 0.24141 Å) of *HT*-$Li_{0.4}$NiB show gradual leaching of Li due to reaction of Li with the silica capillary. Increasing the temperature causes the transformation sequence *HT*-$Li_{0.4}$NiB → *HT*-LiNiB → $LiNi_3B_{1.8}$ → Ni_4B_3.

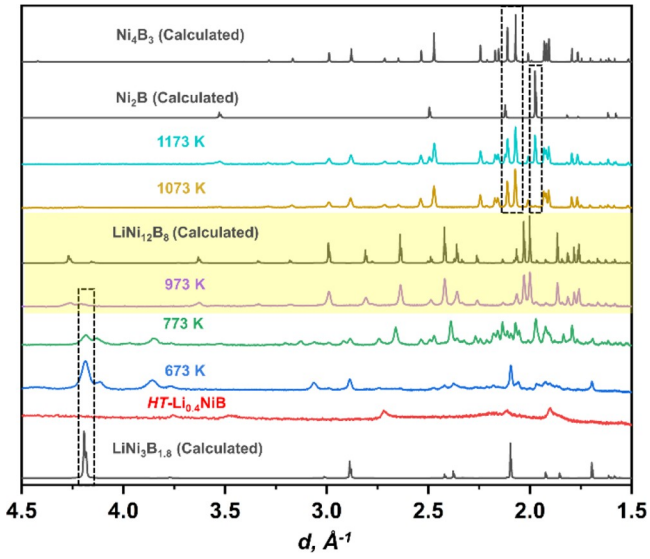

Figure 3. PXRD patterns (λ = 1.540593 Å) of the ex situ heat treatment of *HT*-$Li_{0.4}$NiB at different temperatures with a 12 h dwelling time. Dotted boxes are placed around the most intense peaks of phases present at specific temperatures.

https://doi.org/10.1021/acsmaterialsau.2c00033
ACS Mater. Au 2022, 2, 614−625

to 973 K, a new set of unknown peaks appear, different from the peaks observed at 773 K (highlighted in yellow in Figure 3), in addition to minor amounts of $LiNi_3B_{1.8}$ and Ni_2B. Upon solving the crystal structure, these unknown peaks are attributed to the novel compound $LiNi_{12}B_8$. Although ex situ heating of *HT*-$Li_{0.4}NiB$ leads to crystalline $LiNi_{12}B_8$ with a high yield, only traces of it form upon heating *RT*-$Li_{0.6}NiB$ at 973 K (Figure S4). Such yield differences most likely arise from the different topologies of the [NiB] layers in the partially Li-deintercalated precursors.[38,39]

Interestingly, the formation of $LiNi_{12}B_8$ is observed only during the ex situ experiment and not upon in situ heating, suggesting that the dwelling time plays a crucial role in stabilizing the target compound. The importance of time–temperature regimes for crystallization processes was previously established.[54,55] Therefore, we have investigated the impact of dwelling time on the preparation of $LiNi_{12}B_8$ to shed light on the reaction kinetics and optimize the yield. For this, *HT*-$Li_{0.4}NiB$ was sealed in Nb tubes and heated to 973 K (heating rate of 1.4 K/min) with variable dwelling times (Figure S5). Ex situ dwelling at 973 K for 8 h results in the target $LiNi_{12}B_8$ phase with $LiNi_3B_{1.8}$ as a side product (~10 wt % from the Rietveld refinement of PXRD data). The significant amount of $LiNi_3B_{1.8}$ indicates that a longer dwelling time might be required. When the dwelling time is increased to 12 h, $LiNi_{12}B_8$ becomes the primary phase with $LiNi_3B_{1.8}$ (~3 wt %) and Ni_2B (~0.5 wt %) as minor impurities. When the dwelling time is set to 16 h, a significant amount of Ni_2B is detected (~22 wt %) along with the target phase and traces of $LiNi_3B_{1.8}$. The concurrent appearance of $LiNi_{12}B_8$ and Ni_2B from $LiNi_3B_{1.8}$ implies that $LiNi_3B_{1.8}$ (Ni/B = 1.67:1) disproportionates into Ni-rich Ni_2B (Ni/B = 2:1) and Ni-deficient $LiNi_{12}B_8$ (Ni/B = 1.5:1). Our results suggest that a 12 h dwelling time is an adequate compromise to obtain the highest yield of the target $LiNi_{12}B_8$ compound (Figures 4 and S5). Hence, the crystallization of $LiNi_{12}B_8$ from the semicrystalline *HT*-$Li_{0.4}NiB$ phase depends not only on the dwelling temperature but also on the dwelling time. Even though the formation of the $LiNi_{12}B_8$ compound is witnessed upon ex situ heating of *HT*-$Li_{0.4}NiB$, this compound cannot be synthesized via direct synthesis from the elements, further emphasizing the metastable nature of $LiNi_{12}B_8$ (Figure S6).

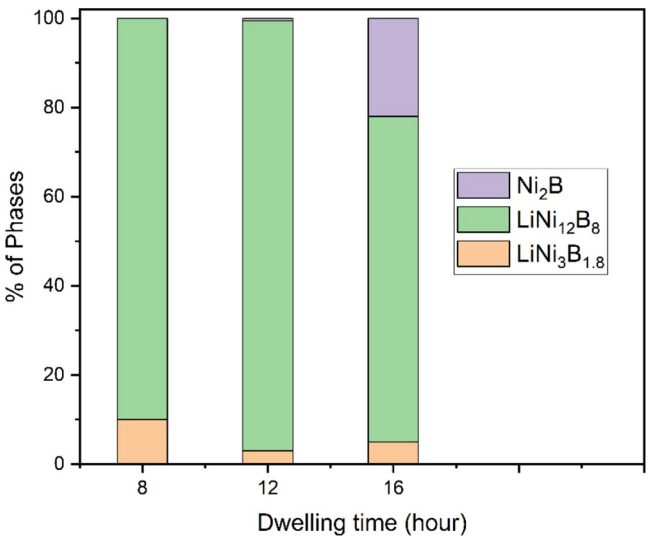

Figure 4. Contents of phases $LiNi_3B_{1.8}$, Ni_2B, and $LiNi_{12}B_8$ upon ex situ heating of *HT*-$Li_{0.4}NiB$ at 973 K for variable dwelling times; 12 h dwelling time is optimal with respect to the content of side phases.

From the analysis of both in situ and ex situ experiments, we can conclude that thermal energy increases the mobility of Li ions in both *RT*-$Li_{0.6}NiB$ and *HT*-$Li_{0.4}NiB$ and stabilizes the Li depleted compounds, $LiNi_3B_{1.8}$, $LiNi_{12}B_8$, and finally stable binary borides of nickel (Ni_3B and Ni_4B_3). The basic pH of the solution obtained upon washing the samples with DI water supports the release of elemental Li with the subsequent formation of LiOH. However, complete deintercalation of Li to form NiBene layers cannot be achieved under the thermal methods employed.

In situ high-temperature PXRD data are utilized to reveal the metastable nature of $LiNi_{12}B_8$. Upon heating $LiNi_{12}B_8$, no visible changes in the PXRD patterns are detected (Figure S7) until 815 K, when diffraction peaks for Ni_4B_3 appear. At 983 K, $LiNi_{12}B_8$ irreversibly decomposes into Ni_4B_3 and does not reform on cooling to room temperature. Similarly, the formation of Ni_4B_3 is observed when the DI water-washed $LiNi_{12}B_8$ phase is heated ex situ at 973 K for 12 h in a sealed niobium container. The formation of only Ni_4B_3 (Ni/B = 1.33:1) upon ex situ heating is in line with the Ni/B ratio in the $LiNi_{12}B_8$ compound (Ni/B = 1.5:1), further supporting the proposed (vide infra) structural model. Therefore, upon exposing LiNiB (*RT*- and *HT*-) compounds to the air, deintercalation of Li atoms takes place, stabilizing metastable $Li_{\sim 0.5}NiB$ compounds, which then form $LiNi_{12}B_8$ upon heating and finally decomposing completely to Ni_4B_3 (Scheme 1).

Scheme 1. Schematic Showing That $LiNi_{12}B_8$ Can Be Only Obtained via Gradual Leaching of Li upon Heating of the Layered $Li_{\sim 0.5}NiB$ Precursor[a]

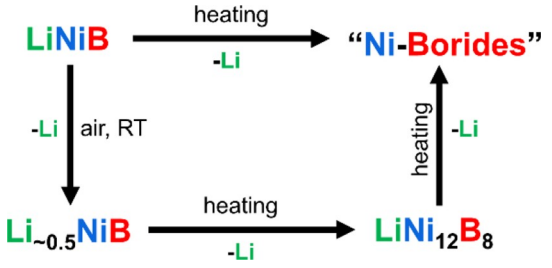

[a]The latter is a result of partial Li deintercalation from LiNiB.

4. CRYSTAL STRUCTURE

The formation of $LiNi_{12}B_8$ is sensitive to annealing temperature and dwelling time. $LiNi_{12}B_8$ compounds can only be accessed by ex situ heating of a microcrystalline *HT*-$Li_{0.4}NiB$ precursor, yielding microcrystalline powder of the target compound. Several attempts to grow crystals large enough for single-crystal XRD were unsuccessful. As a result, the crystal structure of $LiNi_{12}B_8$ was solved from the high-resolution synchrotron PXRD data, using the FOX software[56] and further refined with GSAS II software.[57] $LiNi_{12}B_8$ crystallizes in a tetragonal unit cell, space group *I4/mmm* (a = 10.55673(9) Å, c = 10.00982(8) Å, V = 1115.54(3) Å^3, Z = 6, Pearson symbol *tI*126) (Table 1). Searches for the Pearson symbol, unit cell metric, and Wyckoff sequence ($omn^2h^2jidecb$) in the Inorganic Crystal Structure Database (ICSD)[58] indicate that $LiNi_{12}B_8$ forms a new structure type. Upon least-square refinements, the occupancy factors of selected Ni sites deviate

https://doi.org/10.1021/acsmaterialsau.2c00033
ACS Mater. Au 2022, 2, 614–625

Table 1. Experimental Details and Crystallographic Data for the $Li(Ni_{12-x}Li_x)B_8$ (x = 0.317(2)) Compound[a]

empirical formula	$Li(Ni_{12-x}Li_x)B_8$ (x = 0.317(2))
formula weight, g/mol	4688.42
space group, Z	$I4/mmm$, 6
cell parameters	
a, Å	10.55673(9)
c, Å	10.00982(8)
V, Å^3	1115.54(3)
temperature, K	295
wavelength, Å	0.45784
step scan, °	0.001
2θ° range	2.5−50
program	GSAS II
R_B	0.066
R_P	0.063
G.O.F.	1.196

[a]Rietveld refinement was done using high-resolution synchrotron powder X-ray diffraction data (11-BM APS ANL). Further details of the crystal structure refinement can be obtained from the Inorganic Crystal Structure Database (ICSD) produced by FIZ Karlsruhe − Leibniz Institute for Information Infrastructure (www.fiz-karlsruhe.de) by quoting the CSD-2158021 deposition number at www.ccdc.cam.ac.uk/structures.

from unity, suggesting mixed Ni/B or Ni/Li site occupancies. From the crystal structure analysis, the refined interatomic distances between Ni sites (~2.5−2.6 Å) are too long for the small B atoms; thus, mixed occupied Ni/Li sites are considered. The least-square refinements suggested five Ni/Li mixed occupied sites, 32o, 16m, 8h, 4d, and 4e, with Li occupancies ranging 2−8% (Table S1). Refinement of this model from the high-resolution synchrotron PXRD data resulted in R_B = 6.6% and G.O.F = 1.196 (Figure S8, Table 1). With the consideration of five Ni/Li mixed occupied sites, the formula refines to $Li_{1.317(2)}Ni_{11.683(2)}B_8$ or $Li(Ni_{12-x}Li_x)B_8$ (x = 0.317(2)), which is in excellent agreement with the Li/Ni ratio of $Li_{1.4(3)}Ni_{11.6(2)}$ determined from the ICP-MS data (see the Experimental Section in Supporting information). For the sake of clarity, we will refer to the title compound as $LiNi_{12}B_8$. Several reactions targeting the refined composition of $LiNi_{12}B_8$ were attempted by utilizing elemental precursors and LiH or Li as the lithium sources (Figure S6), but the $LiNi_{12}B_8$ phase could not be obtained, thereby emphasizing its metastability.

The crystal structure of $LiNi_{12}B_8$ can be described by either a framework of Li- or B-centered Ni polyhedra. In addition to five Ni/Li mixed occupied sites, there are two fully occupied Li sites (Figure 5), Li1 at the 4c position and Li2 at the 2b position, each inside cuboctahedra of 12 Ni atoms. The Li−Ni bond distances are in the range of 2.50−2.66 Å, comparable to Li−Ni distances in the known Li−Ni−B compounds.[39,53,59] The Li-centered nickel polyhedra are connected by corner sharing; however, Li2-centered polyhedra are separated from each other by two face-shared Ni-centered rectangular prisms (Figure 5d).

There are four different types of B atoms present in the crystal structure: B1 atoms in the 16n position are coordinated by eight Ni atoms in a square antiprismatic environment; B2 atoms occupy the 16n site that has seven nearest Ni atoms forming a capped trigonal prism; B3 atoms occupy 8h sites with six nearest Ni atoms in a trigonal prism, and B4 atoms at 8i sites are coordinated by eight Ni atoms forming a square antiprism (Figure 6a−e). The Ni−B bond distances are in the

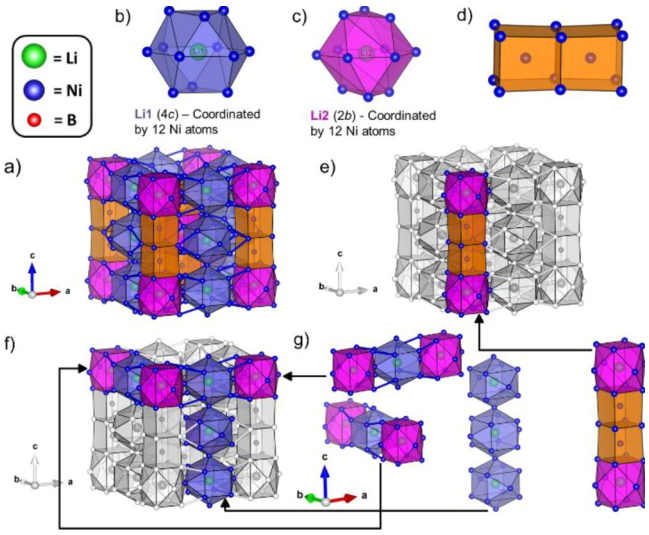

Figure 5. (a) Polyhedral representation of the $LiNi_{12}B_8$ crystal structure in terms of Li-centered Ni polyhedra (deep blue and magenta) and Ni-centered rectangular prisms (orange); (b) Li1-centered nickel polyhedron; (c) Li2-centered nickel polyhedron; (d) two Ni-centered rectangular prisms, connected by face sharing, separate the Li2-centered polyhedra; and (e−g) different building blocks are highlighted within the structure. B atoms are omitted for clarity.

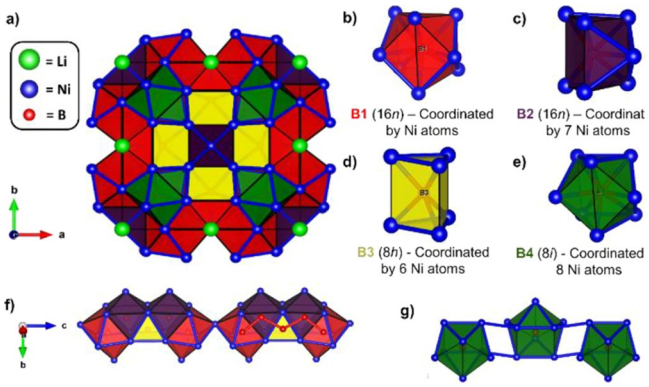

Figure 6. (a) Crystal structure of $LiNi_{12}B_8$ represented as boron-centered Ni polyhedra. Coordination environment of (b) B1; (c) B2; (d) B3; and (e) B4. (f) B1-, B2-, B3-centered polyhedra are connected by face sharing, resulting in B_5 chains (one such chain is drawn in red on top of the polyhedra, right); (g) B4-centered polyhedra are linked by corner sharing.

range of 2.04−2.26 Å and are comparable to the Ni−B distances found in binary nickel borides[60−62] and ternary Li−Ni−B borides.[39,53,59] The crystal structure of the $LiNi_{12}B_8$ compound can be represented as a framework of B-centered 6-, 7-, and 8-vertex polyhedra of Ni atoms, as shown in Figure 6a−e. Here, the B4-centered polyhedra are linked together by two Ni−Ni bridges (Figure 6g). B1-, B2-, and B3-centered polyhedra are connected by face sharing, resulting in B_5 zig-zag chains (B1−B2−B3−B2−B1) (Figures 6f and S9) with B−B distances of 1.80−1.82 Å. These B−B distances are comparable to that found in elemental boron and other binary and ternary borides.[39,53,59,63−66]

Interestingly, a similar kind of zig-zag [B_5] chain is observed in the crystal structure of $Ni_{12}AlB_8$,[67] which is orthorhombic (space group $Cmce$, a = 10.5265 Å, b = 14.527 Å, c = 14.5540 Å, Z = 12) with nine distinct B sites as opposed to tetragonal

https://doi.org/10.1021/acsmaterialsau.2c00033
ACS Mater. Au 2022, 2, 614−625

$LiNi_{12}B_8$ with four distinct B sites (Figure S10). Like $LiNi_{12}B_8$, the different B sites in the structure of $Ni_{12}AlB_8$ are surrounded by six, seven, and eight Ni atoms, with similar coordination environments. Comparison of the Li and Al-centered Ni polyhedra in $LiNi_{12}B_8$ and $Ni_{12}AlB_8$ reveals similar coordination environments (Figures 6 and S10); however, the building blocks are oriented differently, differentiating one structure from the other (Figures 5 and S11). Besides their structural dissimilarities, the synthetic procedures to obtain $LiNi_{12}B_8$ and $Ni_{12}AlB_8$ also differ. $Ni_{12}AlB_8$ can be obtained by a direct reaction from the element, but lower temperature annealing (1173−1223 K) is needed to stabilize $Ni_{12}AlB_8$, while higher temperatures (>1223 K) favor the formation of the τ-boride $Ni_{20}Al_{3-x}B_{6+4x}$, x = 1.5−2.[67]

5. ELECTRON MICROSCOPY

The complex structure of $LiNi_{12}B_8$ was solved from the synchrotron PXRD data. An excellent fit of PXRD data to the structural model (Figure S8), sensible interatomic distances and typical coordination environments in the obtained structural model upholds the structural solution. To further confirm the structural model of $LiNi_{12}B_8$, we used ED and STEM. ED patterns collected from the main crystallographic zones [001], [100], [110], and [111] (Figure 7a) confirm the tetragonal symmetry with $a \sim 10.5$ Å and $c \sim 10.0$ Å. Although the values of a and c are close, the high-angle annular dark field (HAADF) STEM images of [001] and [100] zones and their corresponding simulated images differ significantly (Figure 8), in agreement with tetragonal symmetry. Similar values of a and c parameters in a tetragonal structure can render this structure as "pseudo-cubic", therefore causing twinning. Such twinning and corresponding twin boundaries are observed in ED patterns and HAADF-STEM images (Figure 7b) for the [100] zone, where two grains are flipped along the <011> plane resulting in the splitting of diffraction spots in the [100] ED pattern (Figure 7b, inset).

The observed intensity for a HAADF-STEM image is directly proportional to the atomic number squared so that heavier atoms (Ni, in this case) appear brighter, while light atoms (Li and B) are essentially invisible. On the contrary, light atoms (Li and B) can be visualized in ABF-STEM images and appear as dark gray dots together with darker Ni atoms. HAADF-STEM images for the five main crystallographic zones ([001], [100], [101], [110], and [111]) are shown in Figure 8 along with the simulated images and corresponding structure overlays, where Ni or Ni/Li sites are depicted as dark-blue spheres and Li as yellow spheres. The simulated and experimental HAADF-STEM images match extremely well, confirming the positions of Ni atoms in the structural model obtained from synchrotron PXRD data. In addition, the columns built from Ni atoms are emphasized in Figure 8. The characteristic distances between these columns along the different directions determined from the HAADF-STEM images are 0.73 nm for [001], 0.75 nm for [100], 0.5 nm for [101], 0.5 nm for [110], and 0.26 nm for [111] zones, which align excellently with the expected values from the structural model. Since HAADF-STEM images are dominated by heavier atoms (here Ni), structural models with a similar Ni environment cannot be distinguished. Owing to this, HAADF-STEM images were not useful in differentiating ideal ($LiNi_{12}B_8$, without Li/Ni mixed occupied sites) and disordered ($Li(Ni_{12-x}Li_x)B_8$ with Li/Ni mixed occupied sites) structural models.

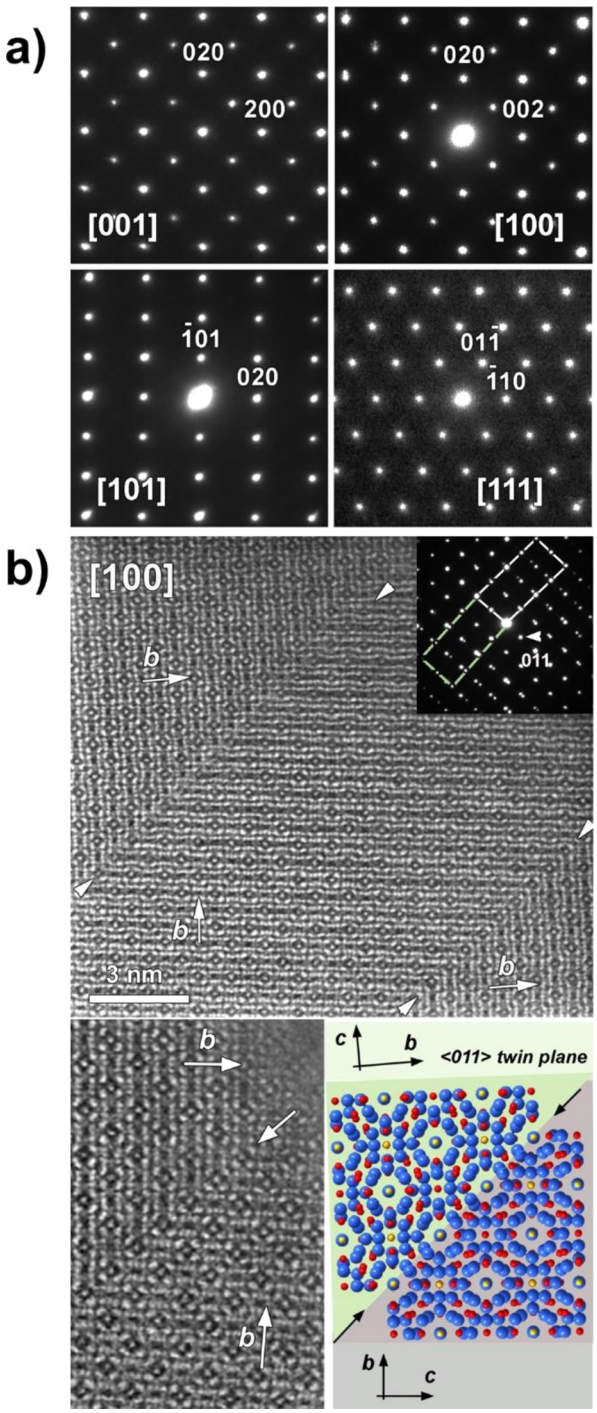

Figure 7. (a) Electron diffraction patterns of the four main zones of tetragonal $LiNi_{12}B_8$ structure. (b) Antiphase boundary defect along the <011> plane visible from the ED pattern of the [100] zone and HAADF image. Ni and Ni/Li sites are shown in blue, Li sites in yellow, and B sites in red.

On the other hand, the ABF STEM analysis is suitable for imaging light elements. Thus, ABF-STEM images were acquired to better visualize positions of lighter atoms (Li and B) in the structure. The ABF-STEM image in the [110] crystallographic zone is consistent with the simulated image (Figure S12), confirming the proposed structural model. However, given the complexity of the structure and that the STEM images are 2D projections of the structure, we cannot resolve the intricate Ni/Li disorder using STEM since for all of

https://doi.org/10.1021/acsmaterialsau.2c00033
ACS Mater. Au 2022, 2, 614−625

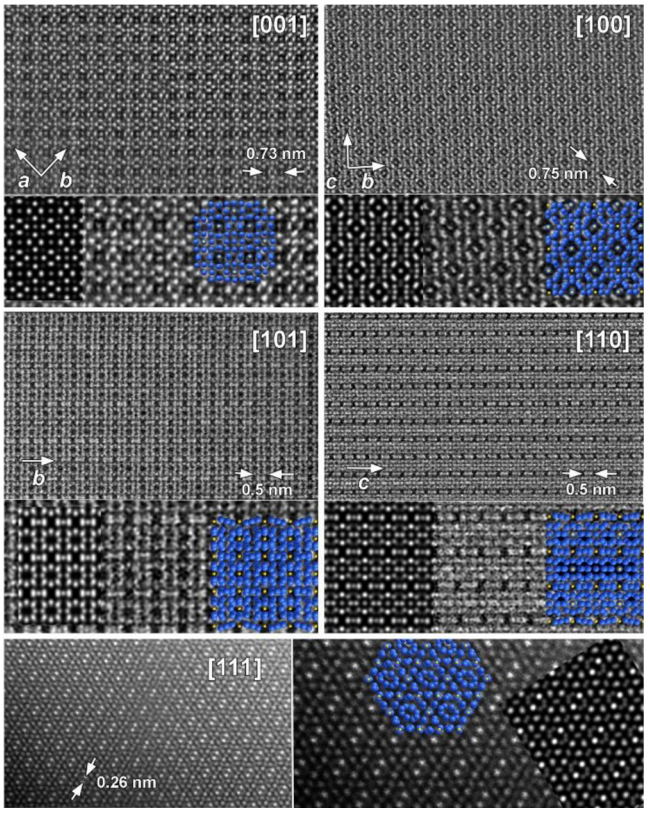

Figure 8. High-resolution HAADF-STEM images of the five main zones with magnified images, simulated patterns of the $LiNi_{12}B_8$ structure, and the structure overlays. Ni and Ni/Li sites are shown in blue, and Li sites, in yellow.

the crystallographic viewing zones, the Ni and Li sites are located within the same column when viewed in the 2D projections.

A plate-like crystallite morphology of $LiNi_{12}B_8$ is evident from SEM images (Figure S13). Energy-dispersive X-ray analysis (EDX) verifies the presence of only Ni and B, whereas detection of Li and accurate quantification of B cannot be performed due to limitations of the EDX technique. Signals for Nb (container used for synthesis) or any other heavy elements besides Ni are not detected in the sample, proving that $LiNi_{12}B_8$ is not a Nb-stabilized phase. The homogeneous distribution of Ni and B atoms can be clearly seen from the false-color elemental maps collected from different sample areas (Figure S13).

6. SOLID-STATE NMR SPECTROSCOPY

HAADF-STEM was extremely useful in confirming the proposed structural model but only with respect to the atomic positions of heavy Ni atoms. We further utilized ^{7}Li and ^{11}B solid-state magic angle spinning (MAS) NMR spectroscopy to confirm the positions of light atoms in the structure. There are seven crystallographically independent Li sites, with five of those sites being mixed occupied by Li/Ni. There are four crystallographically independent B sites in the structure. Importantly, both MAS ^{7}Li and ^{11}B NMR spectra of $LiNi_{12}B_8$ are distinct from the NMR spectra of other known ternary borides in the Li−Ni−B system (Figure S14).[39,53,59] In the MAS ^{7}Li solid-state spectra (Figure 9), a total of eight peaks are observed, two of them are attributed to the two fully occupied Li sites in the $LiNi_{12}B_8$ structure (marked in red).

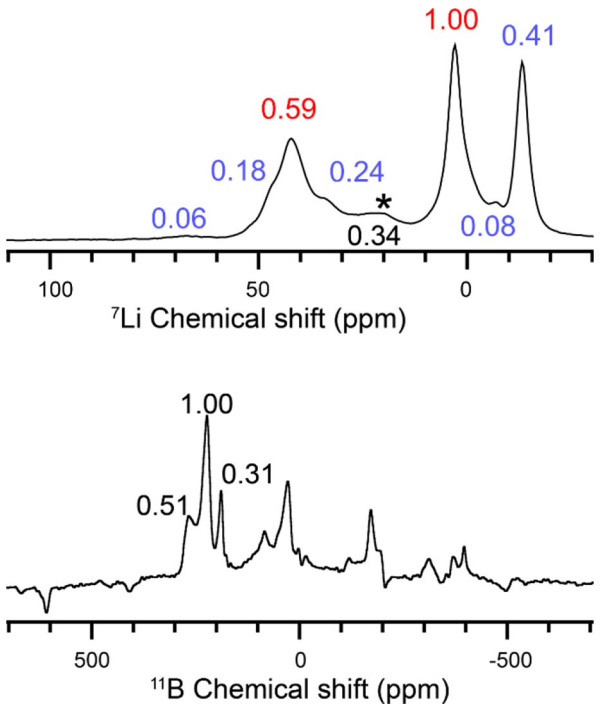

Figure 9. ^{7}Li (top) and ^{11}B (bottom) solid-state NMR spectra of the $LiNi_{12}B_8$ compound. In the ^{7}Li NMR spectra, the peaks marked in red are considered for two fully occupied Li sites, five peaks marked in blue are for the five Li/Ni mixed occupied sites, and the peak in black marked with an asterisk is for the impurity $LiNi_3B_{1.8}$ phase. Experiments were performed at 9.4 T and 25 kHz MAS.

The peak around 22 ppm (marked with *) corresponds to the small amount of the impurity phase $LiNi_3B_{1.8}$ (Figures 9 and S14).[67] The remaining five peaks (marked in blue) in the ^{7}Li NMR spectra are assigned to the five Li/Ni mixed occupied sites within the $LiNi_{12}B_8$ phase. Considering the multiplicity of each Li/Ni (M) occupied site and the two fully occupied Li sites (Table S1), the expected integrated intensity values for $LiNi_{12}B_8$ are M1/M2/M3/M4/M5/Li1/Li2 = 0.896(3):0.352(4):0.152(3):0.34(5):0.152(5):4: 2 or 0.224:0.088:0.038:0.085:0.038:1:0.5, when scaled to unity. From the MAS NMR spectrum, the peak intensities' qualitative ratio is 0.41:0.24:0.08:0.18:0.06:1:0.59 (Figure S15), which is in somewhat reasonable agreement with the proposed model obtained by XRD refinements. However, given the significant overlap of ^{7}Li peaks in the spectrum, it is challenging to perform quantitative integration/deconvolution. Yet, the presence of more than two MAS NMR ^{7}Li peaks is in line with the disorder associated with Li/Ni mixed occupancies, rather than the fully ordered $LiNi_{12}B_8$ structure with only two Li sites. The MAS ^{7}Li NMR chemical shifts for all eight peaks are in the range of −20 to +70 ppm, indicating a Knight shift from the conduction electrons and suggesting the metallic conductivity of the $LiNi_{12}B_8$ phase.[59] This behavior is in good agreement with the predicted metallic behavior from the band structure and electronic density of states (vide infra) (Figure 10). Therefore, the solid-state ^{7}Li NMR spectrum supports the proposed structure and metallic behavior of $LiNi_{12}B_8$.

^{11}B NMR spectra were acquired with two MAS frequencies to confirm the assignment of three distinct isotopic peaks in the $LiNi_{12}B_8$ compound (Figures 9 and S16). The proposed structural model has four independent crystallographic B sites. This discrepancy can be accounted for by considering the

https://doi.org/10.1021/acsmaterialsau.2c00033
ACS Mater. Au 2022, 2, 614−625

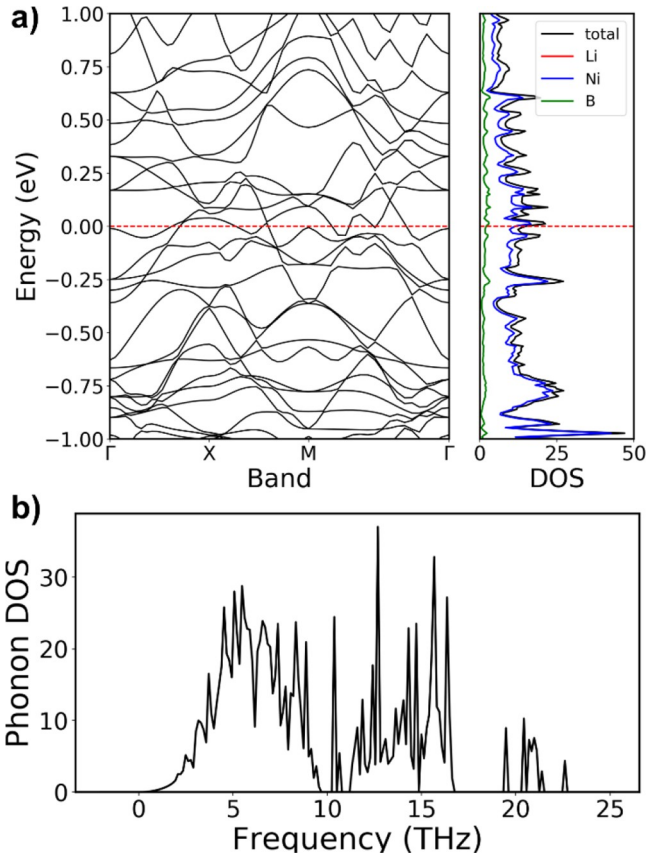

Figure 10. (a) Band structure and electronic density of states (red dashed line indicates the fermi level); (b) phonon density of states.

coordination environment of boron atoms. In the proposed structural model, B1 and B4 atoms, from 16*n* and 8*h* Wyckoff sites, respectively, have the same coordination environment (square antiprismatic polyhedra), consisting of eight Ni atoms. Since atoms in a similar chemical environment likely have similar chemical shifts, these two boron atoms probably generate peaks in the same chemical shift range. Taking into account this assumption and the multiplicity of B1 and B4, the expected ratio of integrated intensities of B peaks in the NMR should be (B1 + B4)/B2/B3 = (16 + 8):16:8 or 1:0.667:0.333 (scaling to unity). These values are in good agreement with the qualitative integrations (1:0.51:0.31) obtained by fitting the isotropic ^{11}B peaks in the solid-state ^{11}B NMR spectrum (Figure S17). Due to the complex interplay between ^{11}B quadrupolar coupling, Knight shift anisotropy, and dipolar coupling, quantitative fitting of the spectrum is challenging. Nevertheless, the range of ^{11}B chemical shift of 190−290 ppm for the $LiNi_{12}B_8$ compound is consistent with its metallic behavior, which in turn is in line with the calculated band structure (vide infra) (Figure 10) and ^{7}Li NMR spectrum.

7. ELECTRONIC AND PHONON STRUCTURE

To assess the thermodynamic stability of the ideal (without Li−Ni mixed occupied sites) $LiNi_{12}B_8$ compound, formation energy is calculated by the DFT calculations. The proposed structural model of the $LiNi_{12}B_8$ compound is stable with a negative formation energy of −308 meV/atom. This formation energy is very close to the formation energy value reported for the *RT*-LiNiB (−339 meV/atom) and *HT*-LiNiB (*RT*-LiNiB (−314 meV/atom)).[39] According to the electronic structure calculations (Figure 10), the compound is predicted to be metallic, which agrees with the Knight shifts in ^{7}Li and ^{11}B NMR spectra. The 3d atomic orbitals of Ni significantly contribute to the electronic density of states, followed by a contribution from 2p atomic orbitals for B, while the contribution of 2s Li atomic orbitals is negligible (Figure S18). The proposed structure of the $LiNi_{12}B_8$ compound is dynamically stable since no imaginary phonon frequencies are observed in the calculated phonon spectrum (Figure 10b).

8. MAGNETIC PROPERTIES

Studies of the magnetic properties of $LiNi_{12}B_8$ are of interest due to an extended Ni framework in its crystal structure with an overall high fraction of the 3d metal. According to the temperature dependence of the molar magnetic susceptibility plot, the title compound displays paramagnetic behavior in the 30−300 K temperature range (Figure 11a,c,d). An abrupt increase in magnetic susceptibility below ∼24 K with the decreasing temperature suggests magnetic ordering (Figure 11a). Additionally, in the low-temperature region (<30 K), the divergence of field-cooled (FC) and zero-field-cooled (ZFC) data indicates either a degree of ferromagnetic ordering or a superparamagnetic transition, or a spin-cluster, or a spin-glass-like behavior. Given the similarity of the $M(T)$ and $M(H)$ data to our earlier work on *RT*-$Li_{0.6}$NiB and *HT*-$Li_{0.4}$NiB,[38] the cluster- or spin-glass scenario seems more likely in this case (Figure S19). Astonishingly similar magnetic behavior of structurally distinct compounds *HT*-$Li_{0.4}$NiB and $LiNi_{12}B_8$ may arise due to the disorder in the Ni environment, where disorder in *HT*-$Li_{0.4}$NiB arises due to the random distribution of multiple substructures $Li[NiB]_n$ (n = 1, 2, 3); $LiNi_{12}B_8$ features mixed occupied Ni/Li sites (Figure S19). With an increase in the applied magnetic field from 50 to 1000 and 2000 Oe, the ZFC/FC bifurcation temperature decreases from ∼18 to ∼12 K and finally to ∼9 K.

The field dependence of magnetization at 100, 200, and 300 K is linear above 1 T with no tendency for saturation, consistent with paramagnetic behavior (Figure 11b). The very slight nonlinearity of magnetization in the low magnetic field of 0−0.5 T, even at 300 K (Figure S20), could be attributed to the presence of a trace amount of ferromagnetic impurities. However, fundamentally, these samples appear to have significantly less ferromagnetic contamination than the *HT*-$Li_{0.4}$NiB precursor.[38] On the other hand, the hysteresis loop in the magnetization vs field plot at 2 K suggests magnetic ordering at low temperatures. To determine the intrinsic molar magnetic susceptibility of $LiNi_{12}B_8$, χ at T > 100 K, the contribution of ferromagnetic impurities was subtracted by the Honda-Owen method (Figure 11c).[68,69] For this, the M/H vs T data were collected at a high enough magnetic field (2 and 4 T) to fully saturate ferromagnetic impurities (Figure 11d inset) and were linearly extrapolated to an infinite field ($1/H \rightarrow 0$). The content of the ferromagnetic impurity is estimated to be 0.002 wt % of Ni metal (under the detection limit of the PXRD experiment), again showing $LiNi_{12}B_8$ to be less contaminated than the starting material *HT*-$Li_{0.4}$NiB. The intrinsic magnetic susceptibility for $LiNi_{12}B_8$ at T > 100 K was fitted to the modified Curie−Weiss equation (Figure 11d): $\chi = \chi_0 + C/(T - \theta)$ where $\chi_0 = 6.938(3) \times 10^{-4}$ emu mol^{-1}, $C = 1.004(7) \times 10^{-1}$ emu K mol^{-1}, and $\theta = 39.2(4)$ K. The positive value of the temperature-independent contribution, χ_0, is consistent with a Pauli-paramagnetic (metallic) contribution, as seen by the calculated electronic band structure and Knight shifts in ^{7}Li

https://doi.org/10.1021/acsmaterialsau.2c00033
ACS Mater. Au 2022, 2, 614−625

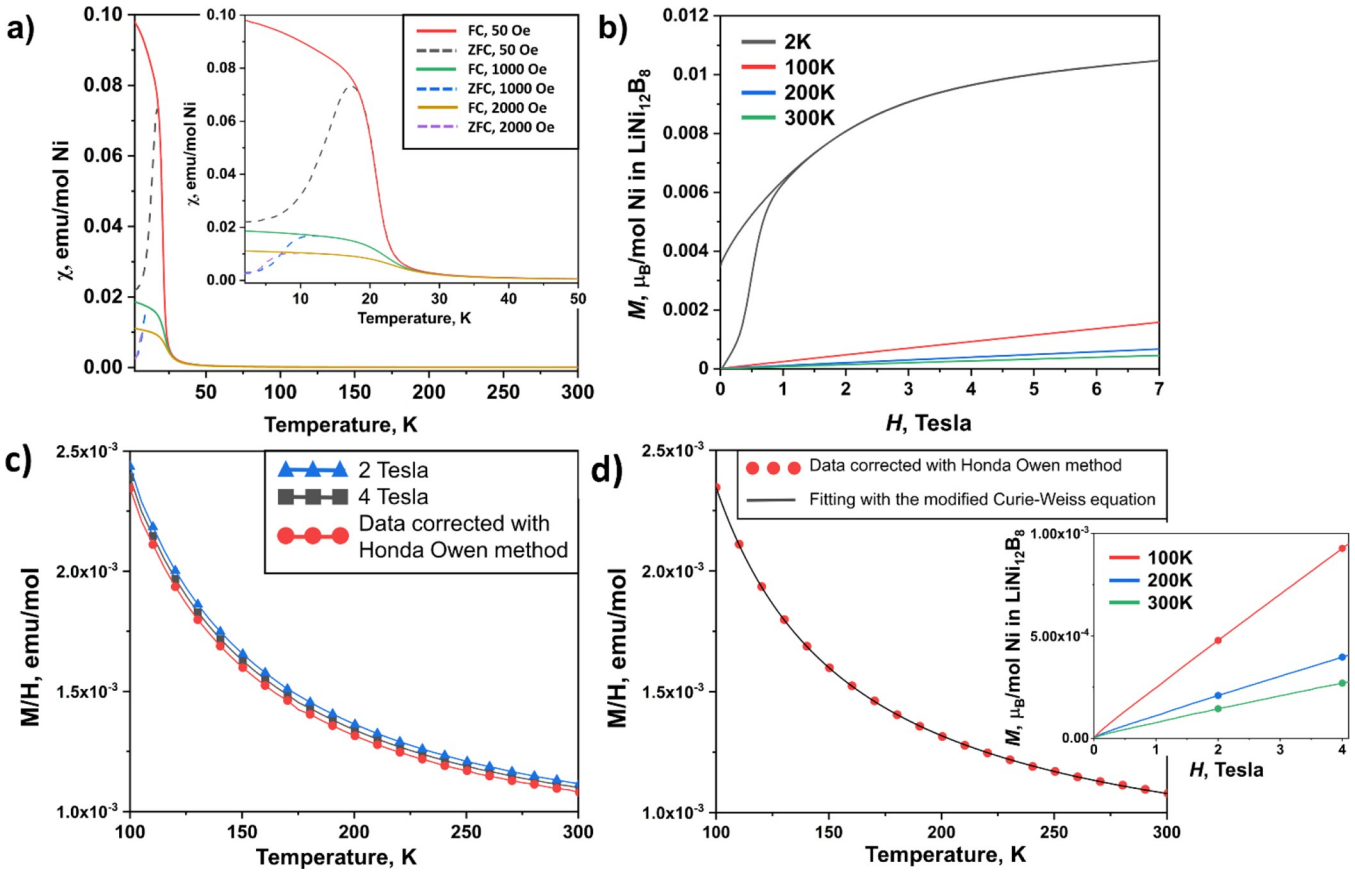

Figure 11. (a) Temperature-dependent ZFC/FC molar susceptibility of the polycrystalline $LiNi_{12}B_8$ sample in the 2−300 K temperature range. Inset: temperature-dependent molar susceptibility in the 2−50 K temperature range; (b) field-dependent magnetization at 2, 100, 200, and 300 K; (c) using M/H vs T data at 2 and 4 Tesla, the contribution from ferromagnetic impurity (estimated to be <0.01%) was calculated by the Honda-Owen method to obtain the intrinsic susceptibility of the $LiNi_{12}B_8$ compound. (d) Data corrected with the Honda Owen method were fitted with the modified Curie−Weiss equation. Inset: M vs H plots in the 0−4 Tesla range for 100, 200, and 300 K temperatures.

and ^{11}B MAS NMR spectra. The positive value of the Weiss constant, θ, indicates weak ferromagnetic coupling between the adjacent Ni spins. The magnetic moment per Ni atom, calculated from the Curie constant, C, amounts to 0.90(1) μ_B/ per f.u., which becomes 0.075(1) μ_B/Ni atom. This effective magnetic moment is lower than the effective magnetic moment of Ni metal (0.6 μ_B/Ni) as well as the spin-only magnetic moment of Ni^{2+} (2.83 μ_B) and Ni^{3+} (1.73 μ_B) ions. Compared to the other known ternary borides in the Li−Ni−B system, the μ_B/Ni atom for $LiNi_{12}B_8$ is lower than that of *RT*-$Li_{0.6}NiB$, *HT*-$Li_{0.4}NiB$, and $LiNi_3B_{1.8}$ but higher than that in the $Li_{2.8}Ni_{16}B_8$ phase (Tables S2 and S3).

Interestingly, magnetic ordering manifesting in ZFC/FC splitting at a low temperature and magnetic field is also seen in other ternary compounds in the Li−Ni−B system: *RT*-$Li_{0.6}NiB$, *HT*-$Li_{0.4}NiB$, $LiNi_3B_{1.8}$, and $Li_{2.8}Ni_{16}B_8$.[38,59] For the Li−Ni−B compounds obtained by high-temperature annealing ($LiNi_3B_{1.8}$, $LiNi_{12}B_8$, and $Li_{2.8}Ni_{16}B_8$), the temperature of ZFC/FC splitting at 50 Oe linearly increases with Ni at.%, while LiNiB polymorphs (33.33 at.% Ni) lack such magnetic transition (temperature-independent paramagnets), and *RT*-$Li_{0.6}NiB$ and *HT*-$Li_{0.4}NiB$ obtained by room-temperature deintercalation exhibit a different trend (Figure S21).

9. CONCLUSIONS

In this study, the metastable layered borides *RT*-$Li_{0.6}NiB$ and *HT*-$Li_{0.4}NiB$ obtained by partial Li deintercalation from the LiNiB polymorph at room temperature were further subjected to elevated temperatures to investigate the extent of Li deintercalation and to achieve individual, Li-free 2D NiB layers, NiBenes. We found that heating of *HT*-$Li_{0.4}NiB$ causes the topological transformation of NiBene layers leading to the formation of the novel metastable compound $LiNi_{12}B_8$ with a new tetragonal structure type. After systematic analysis of in situ high-temperature synchrotron and ex situ laboratory PXRD, we determined that the $LiNi_{12}B_8$ phase is extremely sensitive to annealing temperature and dwelling time. We established that $LiNi_{12}B_8$ cannot be synthesized from the direct reaction of elements and irreversibly decomposes above 973 K, indicating that this compound is indeed metastable. The crystal structure of the compound was solved from high-resolution synchrotron PXRD data and further confirmed by HAADF-STEM and ABF-STEM. A synergistic combination of high-resolution synchrotron PXRD, STEM, ICP-MS, and solid-state ^7Li NMR spectroscopy revealed the presence of Ni/Li mixed occupied sites, establishing the formula as $Li(Ni_{12-x}Li_x)B_8$ (x = 0.317(2)). Owing to the presence of an extended Ni framework and a high fraction of 3d-metal, the $LiNi_{12}B_8$ compound exhibits magnetic ordering below 24 K.

This report illustrates unconventional means toward the synthesis of a metastable compound $LiNi_{12}B_8$ and introduces a contemporary twist on traditional structure solution by combining the complementary information provided by an array of characterization techniques. This study illustrates a

https://doi.org/10.1021/acsmaterialsau.2c00033
ACS Mater. Au 2022, 2, 614−625

state-of-the-art recipe to unambiguously solve crystal structures of microcrystalline materials comprising light elements (Li and B) by utilizing divergent techniques (PXRD, STEM, NMR, ICP-MS, DFT) in conjunction. These findings further emphasize the importance of unconventional synthesis methods in accessing novel metastable compounds that are hardly attained by traditional high-temperature solid-state synthesis.

■ ASSOCIATED CONTENT

Supporting Information

The Supporting Information is available free of charge at https://pubs.acs.org/doi/10.1021/acsmaterialsau.2c00033.

Additional tables with crystallographic data, Rietveld refinement plots, structure comparison, ABF-STEM image, and DOS diagrams (PDF)

Crystallographic information file for CSD-215802 (CIF)

■ AUTHOR INFORMATION

Corresponding Author

Julia V. Zaikina − *Department of Chemistry, Iowa State University, Ames, Iowa 50011, United States;* orcid.org/0000-0002-8755-1926; Email: yzaikina@iastate.edu

Authors

Gourab Bhaskar − *Department of Chemistry, Iowa State University, Ames, Iowa 50011, United States*

Volodymyr Gvozdetskyi − *Department of Chemistry, Iowa State University, Ames, Iowa 50011, United States*

Scott L. Carnahan − *Department of Chemistry and Ames Laboratory, US DOE, Iowa State University, Ames, Iowa 50011, United States*

Renhai Wang − *Ames Laboratory, US DOE, Iowa State University, Ames, Iowa 50011, United States; School of Physics and Optoelectronic Engineering, Guangdong University of Technology, Guangzhou 510006, China*

Aishwarya Mantravadi − *Department of Chemistry, Iowa State University, Ames, Iowa 50011, United States*

Xun Wu − *Department of Chemistry and Ames Laboratory, US DOE, Iowa State University, Ames, Iowa 50011, United States*

Raquel A. Ribeiro − *Department of Physics and Astronomy, Iowa State University, Ames, Iowa 50011, United States*

Wenyu Huang − *Department of Chemistry and Ames Laboratory, US DOE, Iowa State University, Ames, Iowa 50011, United States;* orcid.org/0000-0003-2327-7259

Aaron J. Rossini − *Department of Chemistry and Ames Laboratory, US DOE, Iowa State University, Ames, Iowa 50011, United States;* orcid.org/0000-0002-1679-9203

Kai-Ming Ho − *Department of Physics and Astronomy, Iowa State University, Ames, Iowa 50011, United States*

Paul C. Canfield − *Ames Laboratory, US DOE and Department of Physics and Astronomy, Iowa State University, Ames, Iowa 50011, United States*

Oleg I. Lebedev − *Laboratoire CRISMAT, ENSICAEN, CNRS UMR 650814050, Caen 14050, France*

Complete contact information is available at: https://pubs.acs.org/10.1021/acsmaterialsau.2c00033

Author Contributions

The manuscript was written through contributions of all authors. All authors have given approval to the final version of the manuscript.

Notes

The authors declare no competing financial interest.

Further details of the crystal structure refinement can be obtained from the Inorganic Crystal Structure Database (ICSD) by quoting the CSD-2158021 deposition number at www.ccdc.cam.ac.uk/structures.

■ ACKNOWLEDGMENTS

Financial support from the National Science Foundation (DMR 1944551) CAREER award is gratefully acknowledged. A.J.R. and S.L.C. (NMR spectroscopy), P.C.C. (magnetism), and X.W. and W.H. (ICP-MS) were supported by the U.S. Department of Energy (DOE), Office of Science, Basic Energy Sciences, Materials Science and Engineering Division. R.A.R. was supported by the Gordon and Betty Moore Foundation's EPiQS Initiative through Grant GBMF4411. The Ames Laboratory is operated for the U.S. Department of Energy by Iowa State University under contract #DE-AC02-07CH11358. K.-M.H. was supported by the U.S. Department of Energy (D.O.E.), Office of Science, Basic Energy Sciences, Materials Science and Engineering Division, including a grant of computer time at the National Energy Research Scientific Computing Centre (NERSC) in Berkeley, CA. R.W. was supported by the Guangdong Basic and Applied Basic Research Foundation (Grant No. 2021A1515110328 & 2022A1515012174). Use of the Advanced Photon Source at Argonne National Laboratory was supported by the U. S. Department of Energy, Office of Science, Office of Basic Energy Sciences, under Contract No. DE-AC02-06CH11357.

■ ABBREVIATIONS

PXRD	powder X-ray diffraction
SEM	scanning electron microscopy
HAADF STEM	high-angle annular dark field scanning transmission electron microscopy
ABF	annular bright field
EDXS	energy-dispersive X-ray spectroscopy
NMR	nuclear magnetic resonance
DFT	density functional theory
ICP-MS	inductively coupled plasma mass spectrometry

■ REFERENCES

(1) Chamorro, J. R.; McQueen, T. M. Progress toward Solid State Synthesis by Design. *Acc. Chem. Res.* **2018**, *51*, 2918−2925.

(2) Parija, A.; Waetzig, G. R.; Andrews, J. L.; Banerjee, S. Traversing Energy Landscapes Away from Equilibrium: Strategies for Accessing and Utilizing Metastable Phase Space. *J. Phys. Chem. C* **2018**, *122*, 25709−25728.

(3) Aykol, M.; Montoya, J. H.; Hummelshøj, J. Rational Solid-State Synthesis Routes for Inorganic Materials. *J. Am. Chem. Soc.* **2021**, *143*, 9244−9259.

(4) Stein, A.; Keller, S. W.; Mallouk, T. E. Turning Down the Heat: Design and Mechanism in Solid-State Synthesis. *Science* **1993**, *259*, 1558−1564.

(5) Mesoza Cordova, D. L.; Kam, T. M.; Gannon, R. N.; Lu, P.; Johnson, D. C. Controlling the Self-Assembly of New Metastable Tin Vanadium Selenides Using Composition and Nanoarchitecture of Precursors. *J. Am. Chem. Soc.* **2020**, *142*, 13145−13154.

(6) Sun, W.; Dacek, S. T.; Ong, S. P.; Hautier, G.; Jain, A.; Richards, W. D.; Gamst, A. C.; Persson, K. A.; Ceder, G. The thermodynamic scale of inorganic crystalline metastability. *Sci. Adv.* **2016**, *2*, No. e1600225.
(7) Cordova, D. L. M.; Johnson, D. C. Synthesis of Metastable Inorganic Solids with Extended Structures. *Chem. Phys. Chem.* **2020**, *21*, 1345−1368.
(8) Aykol, M.; Dwaraknath, S. S.; Sun, W.; Persson, K. A. Thermodynamic limit for synthesis of metastable inorganic materials. *Sci. Adv.* **2018**, *4*, No. eaaq0148.
(9) Kanatzidis, M. G. Discovery-Synthesis, Design, and Prediction of Chalcogenide Phases. *Inorg. Chem.* **2017**, *56*, 3158−3173.
(10) Berseth, P. A.; Hughes, T. A.; Schneidmiller, R.; Smalley, A.; Johnson, D. C. Low temperature synthesis using modulated elemental reactants: a new metastable ternary compound, Ni_xMoSe_2. *Solid State Sci.* **2002**, *4*, 717−722.
(11) Kovnir, K. Predictive Synthesis. *Chem. Mater.* **2021**, *33*, 4835−4841.
(12) Martinolich, A. J.; Neilson, J. R. Toward Reaction-by-Design: Achieving Kinetic Control of Solid State Chemistry with Metathesis. *Chem. Mater.* **2017**, *29*, 479−489.
(13) Nartowski, A. M.; Parkin, I. P.; MacKenzie, M.; Craven, A. J.; MacLeod, I. Solid state metathesis routes to transition metal carbides. *J. Mater. Chem.* **1999**, *9*, 1275−1281.
(14) Meyer, H. J. Solid state metathesis reactions as a conceptual tool in the synthesis of new materials. *Dalton Trans.* **2010**, *39*, 5973−5982.
(15) Todd, P. K.; Neilson, J. R. Selective Formation of Yttrium Manganese Oxides through Kinetically Competent Assisted Metathesis Reactions. *J. Am. Chem. Soc.* **2019**, *141*, 1191−1195.
(16) Lei, L.; Yin, W.; Jiang, X.; Lin, S.; He, D. Synthetic Route to Metal Nitrides: High-Pressure Solid-State Metathesis Reaction. *Inorg. Chem.* **2013**, *52*, 13356−13362.
(17) Miura, A.; Ito, H.; Bartel, C. J.; Sun, W.; Rosero-Navarro, N. C.; Tadanaga, K.; Nakata, H.; Maeda, K.; Ceder, G. Selective metathesis synthesis of $MgCr_2S_4$ by control of thermodynamic driving forces. *Mater. Horiz.* **2020**, *7*, 1310−1316.
(18) Rognerud, E. G.; Rom, C. L.; Todd, P. K.; Singstock, N. R.; Bartel, C. J.; Holder, A. M.; Neilson, J. R. Kinetically Controlled Low-Temperature Solid-State Metathesis of Manganese Nitride Mn_3N_2. *Chem. Mater.* **2019**, *31*, 7248−7254.
(19) Parkin, I. P. Solid state metathesis reaction for metal borides, silicides, pnictides and chalcogenides: ionic or elemental pathways. *Chem. Soc. Rev.* **1996**, *25*, 199−207.
(20) Wang, L.; Tang, K.; Zhu, Y.; Li, Q.; Zhu, B.; Wang, L. C.; Si, L.; Qian, Y. Solid state synthesis of a new ternary nitride $MgMoN_2$ nanosheets and micromeshes. *J. Mater. Chem.* **2012**, *22*, 14559−14564.
(21) Birkel, C. S.; Mugnaioli, E.; Gorelik, T.; Kolb, U.; Panthöfer, M.; Tremel, W. Solution Synthesis of a New Thermoelectric $Zn_{1+x}Sb$ Nanophase and Its Structure Determination Using Automated Electron Diffraction Tomography. *J. Am. Chem. Soc.* **2010**, *132*, 9881−9889.
(22) Hofmann, K.; Kalyon, N.; Kapfenberger, C.; Lamontagne, L.; Zarrini, S.; Berger, R.; Seshadri, R.; Albert, B. Metastable Ni_7B_3: A New Paramagnetic Boride from Solution Chemistry, Its Crystal Structure and Magnetic Properties. *Inorg. Chem.* **2015**, *54*, 10873−10877.
(23) White, M. A.; Baumler, K. J.; Chen, Y.; Venkatesh, A.; Medina-Gonzalez, A. M.; Rossini, A. J.; Zaikina, J. V.; Chan, E. M.; Vela, J. Expanding the I−II−V Phase Space: Soft Synthesis of Polytypic Ternary and Binary Zinc Antimonides. *Chem. Mater.* **2018**, *30*, 6173−6182.
(24) White, M. A.; Miller, G. J.; Vela, J. Polytypism and Unique Site Preference in LiZnSb: A Superior Thermoelectric Reveals Its True Colors. *J. Am. Chem. Soc.* **2016**, *138*, 14574−14577.
(25) Cable, R. E.; Schaak, R. E. Low-Temperature Solution Synthesis of Nanocrystalline Binary Intermetallic Compounds Using the Polyol Process. *Chem. Mater.* **2005**, *17*, 6835−6841.
(26) Kieslich, G.; Birkel, C. S.; Stewart, A.; Kolb, U.; Tremel, W. Solution Synthesis of Nanoparticular Binary Transition Metal Antimonides. *Inorg. Chem.* **2011**, *50*, 6938−6943.
(27) White, M. A.; Thompson, M. J.; Miller, G. J.; Vela, J. Got LiZnP? Solution phase synthesis of filled tetrahedral semiconductors in the nanoregime. *Chem. Commun.* **2016**, *52*, 3497−3499.
(28) Rosales, B. A.; White, M. A.; Vela, J. Solution-Grown Sodium Bismuth Dichalcogenides: Toward Earth-Abundant, Biocompatible Semiconductors. *J. Am. Chem. Soc.* **2018**, *140*, 3736−3742.
(29) Uppuluri, R.; Sen Gupta, A.; Rosas, A. S.; Mallouk, T. E. Soft chemistry of ion-exchangeable layered metal oxides. *Chem. Soc. Rev.* **2018**, *47*, 2401−2430.
(30) Rouxel, J.; Tournoux, M. Chimie douce with solid precursors, past and present. *Solid State Ionics* **1996**, *84*, 141−149.
(31) Song, X.; Cheng, G.; Weber, D.; Pielnhofer, F.; Lei, S.; Klemenz, S.; Yeh, Y. W.; Filsinger, K. A.; Arnold, C. B.; Yao, N.; Schoop, L. M. Soft chemical synthesis of H_xCrS_2: an antiferromagnetic material with alternating amorphous and crystalline layers. *J. Am. Chem. Soc.* **2019**, *141*, 15634−15640.
(32) Zhou, X.; Wilfong, B.; Vivanco, H.; Paglione, J.; Brown, C. M.; Rodriguez, E. E. Metastable Layered Cobalt Chalcogenides from Topochemical Deintercalation. *J. Am. Chem. Soc.* **2016**, *138*, 16432−16442.
(33) Heising, J.; Kanatzidis, M. G. Exfoliated and Restacked MoS_2 and WS_2: Ionic or Neutral Species? Encapsulation and Ordering of Hard Electropositive Cations. *J. Am. Chem. Soc.* **1999**, *121*, 11720−11732.
(34) Bianco, E.; Butler, S.; Jiang, S.; Restrepo, O. D.; Windl, W.; Goldberger, J. E. Stability and Exfoliation of Germanane: A Germanium Graphane Analogue. *ACS Nano* **2013**, *7*, 4414−4421.
(35) Neilson, J. R.; McQueen, T. M. Bonding, Ion Mobility, and Rate-Limiting Steps in Deintercalation Reactions with $ThCr_2Si_2$-type KNi_2Se_2. *J. Am. Chem. Soc.* **2012**, *134*, 7750−7757.
(36) Woo, K. E.; Wang, J.; Mark, J.; Kovnir, K. Directing Boron−Phosphorus Bonds in Crystalline Solid: Oxidative Polymerization of P═B═P Monomers into 1D Chains. *J. Am. Chem. Soc.* **2019**, *141*, 13017−13021.
(37) Powderly, K. M.; Guo, S.; Mitchell Warden, H. E.; Nguyen, L. T.; Cava, R. J. Metastable β-$NdCo_2B_2$: A Triclinic Polymorph with Magnetic Ordering. *Chem. Mater.* **2021**, *33*, 6374−6382.
(38) Bhaskar, G.; Gvozdetskyi, V.; Batuk, M.; Wiaderek, K.; Sun, Y.; Wang, R.; Zhang, C.; Carnahan, S. L.; Wu, X.; Ribeiro, R. A.; Bud'ko, S. L.; Canfield, P. C.; Huang, W.; Rossini, A. J.; Wang, C. Z.; Ho, K. M.; Hadermann, J.; Zaikina, J. V. Topochemical deintercalation of Li from layered LiNiB: toward 2D MBene. *J. Am. Chem. Soc.* **2021**, *143*, 4213−4223.
(39) Gvozdetskyi, V.; Bhaskar, G.; Batuk, M.; Zhao, X.; Wang, R.; Carnahan, S. L.; Hanrahan, M. P.; Ribeiro, R. A.; Canfield, P. C.; Rossini, A. J.; Wang, C. Z.; Ho, K. M.; Hadermann, J.; Zaikina, J. V. Computationally driven discovery of a family of layered LiNiB polymorphs. *Angew. Chem., Int. Ed.* **2019**, *131*, 16002−16009.
(40) Gogotsi, Y.; Anasori, B. The Rise of MXenes. *ACS Nano* **2019**, *13*, 8491−8494.
(41) Naguib, M.; Kurtoglu, M.; Presser, V.; Lu, J.; Niu, J.; Heon, M.; Hultman, L.; Gogotsi, Y.; Barsoum, M. W. Two-Dimensional Nanocrystals Produced by Exfoliation of Ti_3AlC_2. *Adv. Mater.* **2011**, *23*, 4248−4253.
(42) Alhabeb, M.; Maleski, K.; Anasori, B.; Lelyukh, P.; Clark, L.; Sin, S.; Gogotsi, Y. Guidelines for synthesis and processing of two-dimensional titanium carbide ($Ti_3C_2T_x$ MXene). *Chem. Mater.* **2017**, *29*, 7633−7644.
(43) Barsoum, M. W.; Eklund, P. *The Mn+1AXn Phases: The Precursors for MXenes. In 2D Metal Carbides and Nitrides (MXenes), Structure, Properties and Applications*; Springer: Cham, Switzerland, 2019, 15−35.
(44) Bo, T.; Liu, P. F.; Zhang, J.; Wang, F.; Wang, B. T. Tetragonal and trigonal Mo_2B_2 monolayers: two new low-dimensional materials for Li-ion and Na-ion batteries. *Phys. Chem. Chem. Phys.* **2019**, *21*, 5178−5188.

https://doi.org/10.1021/acsmaterialsau.2c00033
ACS Mater. Au 2022, 2, 614−625

(45) Jiang, Z.; Wang, P.; Jiang, X.; Zhao, J. MBene (MnB): a new type of 2D metallic ferromagnet with high Curie temperature. *Nanoscale Horiz.* **2018**, *3*, 335−341.
(46) Guo, Z.; Zhou, J.; Sun, Z. New two-dimensional transition metal borides for Li ion batteries and electrocatalysis. *J. Mater. Chem. A* **2017**, *5*, 23530−23535.
(47) Jakubczak, M.; Szuplewska, A.; Rozmysłowska-Wojciechowska, A.; Rosenkranz, A.; Jastrzębska, A. M. Novel 2D MBenes—Synthesis, Structure, and Biotechnological Potential. *Adv. Funct. Mater.* **2021**, *31*, No. 2103048.
(48) Wang, J.; Ye, T. N.; Gong, Y.; Wu, J.; Miao, N.; Tada, T.; Hosono, H. Discovery of hexagonal ternary phase Ti_2InB_2 and its evolution to layered boride TiB. *Nat. Commun.* **2019**, *10*, 2284.
(49) Alameda, L. T.; Lord, R. W.; Barr, J. A.; Moradifar, P.; Metzger, Z. P.; Steimle, B. C.; Holder, C. F.; Alem, N.; Sinnott, S. B.; Schaak, R. E. Multi-Step Topochemical Pathway to Metastable Mo_2AlB_2 and Related Two-Dimensional Nanosheet Heterostructures. *J. Am. Chem. Soc.* **2019**, *141*, 10852−10861.
(50) Dahlqvist, M.; Tao, Q.; Zhou, J.; Palisaitis, J.; Persson, P. O. Å.; Rosen, J. Theoretical Prediction and Synthesis of a Family of Atomic Laminate Metal Borides with In-Plane Chemical Ordering. *J. Am. Chem. Soc.* **2020**, *142*, 18583−18591.
(51) Alameda, L. T.; Moradifar, P.; Metzger, Z. P.; Alem, N.; Schaak, R. E. Topochemical Deintercalation of Al from MoAlB: Stepwise Etching Pathway, Layered Intergrowth Structures, and Two-Dimensional MBene. *J. Am. Chem. Soc.* **2018**, *140*, 8833−8840.
(52) Zhou, J.; Palisaitis, J.; Halim, J.; Dahlqvist, M.; Tao, Q.; Persson, I.; Hultman, L.; Persson, P. O. Å.; Rosen, J. Boridene: Two-dimensional $Mo_{4/3}B_{2-x}$ with ordered metal vacancies obtained by chemical exfoliation. *Science* **2021**, *373*, 801−805.
(53) Gvozdetskyi, V.; Sun, Y.; Zhao, X.; Bhaskar, G.; Carnahan, S. L.; Harmer, C.; Zhang, F.; Ribeiro, R. A.; Canfield, P. C.; Rossini, A. J.; Wang, C. Z.; Ho, K. M.; Zaikina, J. V. Lithium Nickel Borides: evolution of MBene layers driven by Li pressure. *Inorg. Chem. Front.* **2021**, *8*, 1675−1685.
(54) Olson, G. L.; Roth, J. A. Kinetics of solid phase crystallization in amorphous silicon. *Mater. Sci. Eng. R Rep.* **1988**, *3*, 1−77.
(55) Naguib, H. M.; Kelly, R. The crystallization of amorphous ZrO_2 by thermal heating and by ion bombardment. *J. Nucl. Mater.* **1970**, *35*, 293−305.
(56) Favre-Nicolin, V.; Černý, R. FOX, 'free objects for crystallography': a modular approach to ab initio structure determination from powder diffraction. *J. Appl. Crystallogr.* **2002**, *35*, 734−743.
(57) Toby, B. H.; Von Dreele, R. B. GSAS-II: the genesis of a modern open-source all purpose crystallography software package. *J. Appl. Crystallogr.* **2013**, *46*, 544−549.
(58) *Inorganic Crystal Structure Database (Web Access), Version 4.2.0*; Fachinformationszentrum Karlsruhe: Germany, 2019. https://icsd.fiz-karlsruhe.de/index.xhtml. Date of access: 05/10/2022. Last accessed: May 12 2022.
(59) Gvozdetskyi, V.; Hanrahan, M. P.; Ribeiro, R. A.; Kim, T.; Zhou, L.; Rossini, A. J.; Canfield, P. C.; Zaikina, J. V. Hydride route to alkali metal borides: a case study of lithium nickel borides. *Chem. − Eur. J.* **2019**, *25*, 4123−4135.
(60) Blum, P. P. The structure of nickel boride NiB. *J. Phys. Radium.* **1952**, *13*, 430−431.
(61) Rundqvist, S.; Pramatus, S.; Lamm, B.; Haug, A.; Theorell, H.; Blinc, R.; Paušak, S.; Ehrenberg, L.; Dumanović, J. Crystal structure refinements of Ni_3B, *o*-Ni_4B_3, and *m*-Ni_4B_3. *Acta Chem. Scand.* **1967**, *21*, 191−194.
(62) Kayser, G. F.; Kayser, F. X. Ni_3B: powder diffraction pattern and lattice parameters. *J. Alloys Compd.* **1996**, *233*, 74−79.
(63) Andersson, S.; Lundström, T.; Andresen, A. F.; Pearson, W. B. The crystal structure of CrB_4. *Acta Chem. Scand.* **1968**, *22*, 3103−3110.
(64) Pauling, L.; Weinbaum, S. The structure of calcium boride CaB_6. *Z. Kristallogr.* **1934**, *87*, 181.
(65) Werheit, H.; Filipov, V.; Shirai, K.; Dekura, H.; Shitsevalova, N.; Schwarz, U.; Armbrüster, M. Raman scattering and isotopic phonon effects in dodecaborides. *J. Phys. Condens. Matter.* **2011**, *23*, No. 065403.
(66) Tanaka, T.; Otani, S.; Ishizawa, Y. Preparation of single crystals of YB_{66}. *J. Cryst. Growth* **1985**, *73*, 31−36.
(67) Ade, M.; Kotzott, D.; Hillebrecht, H. Synthesis and crystal structures of the new metal-rich ternary borides $Ni_{12}AlB_8$, $Ni_{12}GaB_8$, and $Ni_{10.6}Ga_{0.4}B_6$ -examples for the first B_5 zig-zag chain fragment. *J. Solid State Chem.* **2010**, *183*, 1790−1797.
(68) Honda, K. Die thermomagnetischen Eigenschaften der Elemente. *Ann. Phys.* **1910**, *337*, 1027−1063.
(69) Owen, M. Magnetochemische Untersuchungen. Die thermomagnetischen Eigenschaften der Elemente. II. *Ann. Phys.* **1912**, *342*, 657−699.

https://doi.org/10.1021/acsmaterialsau.2c00033
ACS Mater. Au 2022, 2, 614−625